Thermonanomechanics of Graphene Oxide-M13 Bacteriophage Nanocomposites -Towards Graphene-based Nanodevices

Stokes, Kate; Sun, Yiwei; Zhang, Haowei; Passaretti, Paolo; White, Henry; Oppenheimer, Pola Goldberg

DOI:
10.1016/j.cartre.2024.100343

Carbon Trends 15 (2024) 100343

Contents lists available at ScienceDirect

Carbon Trends

journal homepage: www.elsevier.com/locate/cartre

Thermonanomechanics of graphene oxide-M13 bacteriophage nanocomposites -towards graphene-based nanodevices

Kate Stokes [a], Yiwei Sun [a,b,*], Haowei Zhang [c], Paolo Passaretti [d], Henry White [e], Pola Goldberg Oppeneheimer [a,f,*]

[a] School of Chemical Engineering, Advanced Nanomaterials Structures and Applications Laboratories, College of Engineering and Physical Sciences, University of Birmingham, Edgbaston, Birmingham, B15 2TT, UK
[b] Paragraf Limited, Cambridge, PE28 3 EB, UK
[c] School of Physical and Chemical Sciences, Queen Mary University of London, London, E1 4NS, UK
[d] Institute of Cancer and Genomic Sciences, College of Medical and Dental Sciences, University of Birmingham, B15 2TT, UK
[e] BAE-Systems – Air Sector, Buckingham House, FPC 267, Filton, Bristol, UK
[f] Healthcare Technologies Institute, Institute of Translational Medicine, Mindelsohn Way, Birmingham, B15 2TH, UK

ARTICLE INFO

Keywords:
Graphene oxide
M13 bacteriophage
Nano-mechanics
In-situ Raman spectroscopy

ABSTRACT

The self-assembly of graphene oxide (GO) and M13 bacteriophage results in the formation of micro-porous structures, known as GraPhage13 aerogels (GPA). Given the limited applications of aerogels in industry due to their nanomechanical properties, along with the previously observed temperature-dependent characteristics in graphene-based nanocomposites, a thorough exploration of the thermosensitive nanomechanical properties of GPA is essential. Herein, a comprehensive characterisation of the morphology, composition, and spectroscopic analysis of the GPA for a range of temperatures has been conducted and correlated with its nanomechanical properties. Elevated temperatures have been found to lead to gradual removal of oxygen-containing functional groups (OCFGs) from GPA, resulting in increased structural defects and reduced stiffness. Notably, unique nanomechanical behaviours of GPA have been further identified, where the thermal expansion of sp^3 bonds exceeds that of a crystalline sp^3 structure, while the thermal contraction of sp^2 bonds in GPA is found to be between graphite and GO. This underscores the impact of GO functionalisation on the thermal expansion behaviour of GPA. The obtained insights enhance the overall comprehension of the temperature annealing impact on GPA and highlight the tunability of its nanomechanical properties, showcasing a broad potential of this novel nanocomposite across a diverse range of applications.

1. Introduction

Graphene Oxide (GO) is an atomically thin layer of sp^2-hybridised carbon with oxygen-containing functional groups (OCFGs) such as hydroxyl, carboxyl, carbonyl and epoxide [1]. The presence of the OCFGs enables GO to interact with biomolecules, facilitating its self-assembly into graphene-based nanocomposites [2]. These structures have demonstrated a wide range of applications such as in bone tissue engineering [3,4], anti-corrosion coatings [5,6] and drug delivery [7,8]. Previous research has established that GO interacts with the M13 bacteriophage [9,10], a filamentous virus with dimensions of approximately 6.6 nm in width and 880 nm in length [11]. M13 phages comprise of circular-shaped single-stranded DNA, surrounded by a capsid consisting of 2700 copies of the pVIII major coat protein. The minor coat proteins pIII and pVI are present at its head and pVII and pIX at its tail [12]. The self-assembly of GO and M13 enables the fabrication of GraPhage13 aerogels (GPA). These nanocomposites exhibit a porous structure, resulting in a high surface area of 325 $m^2\ g^{-1}$ and ultra-low density of 8.8 mg/cm^3 [9], with the properties of GPA being tuneable for specific applications. Manipulating the genetic and chemical properties of M13 holds considerable potential in altering the characteristics of GPA, including the modification of its binding [13,14] and electrical properties [11,15]. Moreover, the integration of additional nanomaterials into the GPA structure can further enhance its properties, with the integration of carbon nanotubes amplifying the electrical conductivity by a factor of 30 compared to the original GPA [16]. With these

* Corresponding authors.
E-mail addresses: yiwei.sun@qmul.ac.uk (Y. Sun), GoldberP@bham.ac.uk (P. Goldberg Oppeneheimer).

https://doi.org/10.1016/j.cartre.2024.100343
Received 23 January 2024; Received in revised form 13 March 2024; Accepted 13 March 2024
Available online 17 March 2024

prospects, alongside the cost-effective, scalable and environmentally friendly production of GPA [9], it has been continuously establishing itself as an appealing nanomaterial for a broad range of applications ranging from adsorbents [17,18], through electrodes [19,20] and onto sensors [21,22].

To enable the utilisation of aerogels in these applications, they must exhibit excellent mechanical properties including a high mechanical strength and stability, elasticity, durability, and thermal stability [23,24]. However, aerogels often suffer from suboptimal mechanical characteristics such as low mechanical stability, brittleness, and poor deformation recovery, thereby limiting their potential in industrial exploitation [25,26]. Since graphene-based hybrid nanocomposites have previously demonstrated temperature-dependent stability, structure and mechanical properties [27,28], it is imperative to evaluate the influence of temperature on the morphology, composition and nanomechanical properties of GPA to facilitate the comprehensive understanding of GPA's sensitivity to changes in temperature as well as its inherent tunability. Understanding the thermomechanical properties of GPA, especially under varying temperature and related mechanical stress conditions, is critical to ensuring their reliability and efficiency in applications such as electronics, where the devices are heated during operation. This knowledge not only aids in optimising their performance but also opens new possibilities for their use in environments with extreme temperature conditions, *e.g.,* cryogenic applications, or mechanical demands.

In this study, the effects of temperature on the morphology, composition and nanomechanics of GPA were examined through the annealing of the nanocomposite at temperatures ranging from 25 °C to 300 °C. This range is aligned with the commonly applied temperatures for various applications including for instance, low temperature thermal energy storage [29,30], gas sensors [31,32] and carbon capture [33,34]. The morphology and composition of GPA have been subsequently analysed *via* scanning electron microscopy (SEM) and energy-dispersive X-ray spectroscopy (EDX). Furthermore, the nanomechanical properties have been investigated by obtaining force-distance (F-D) curves *via* atomic force microscopy (AFM) and, to gain an in-depth understanding of the effect of temperature on the structure of GPA, Raman spectroscopy with *in-situ* annealing has been performed. The annealing of GPA was found to increase the carbon-to-oxygen (C:O) ratio, modify the presence of crystal defects and reduce both the stiffness of the nanocomposite as well as the adhesion force between it and the AFM probe. The thermal expansion rate of sp^3 bonds in GPA were established to exceed these in a crystalline sp^3 structure, while the sp^2 bonds exhibited thermal expansion behaviour between graphite and GO, signifying the impact of graphene oxide's functionalisation on the thermal expansion of GPA.

This research highlights the improved understanding of the temperature-dependent properties of GPA and elucidates the potential to manipulate its structure, composition and nanomechanics through the heat exposure. Advancing our understanding of GPA, a carbon-based aerogel, utilising its enhanced thermal and nanomechanical properties, make it a promising candidate for environmental applications including water purification systems and air filtration as well as in the development of smart materials for sensors and actuators.

The findings collectively not only contribute to the expanding body of knowledge on carbon materials, offering insights pertinent to a broad range of applications ranging from nanotechnology to environmental engineering but also emphasise the ability to fine-tune the GPA, paving the way for the integration of this novel nanocomposite in graphene-based devices for applications in for instance, electromagnetic wave absorption [35,36], oil-water separation [37,38] or thermal energy storage [39,40].

2. Materials and methods

2.1. Propagation and purification of M13 bacteriophage

The protocol for propagating and purifying the M13 bacteriophage has been adopted from Stokes *et* al. [10]. In brief, M13 bacteriophage (New England Biolabs, UK) was propagated using One Shot TOP10F' Chemically Competent *Escherichia coli* (*E.coli*) (Thermo Fisher Scientific). Initially, *E.coli* cells were cultivated by inoculating nutrient broth (NB) agar (Sigma) plates and incubating them overnight at 37 °C. The *E. coli* was then transferred from the petri dishes into 50 mL falcon tubes containing Nutrient Broth (NB) and tetracycline (Sigma) dissolved in ethanol to achieve a final concentration of 5 μg/ml. These tubes were placed in a shaker incubator and incubated overnight at 37 °C, 150 rpm. This *E.coli*-NB-tetracycline solution was directly used for the M13 propagation process. M13 was incubated overnight in NB along with the *E.coli*-NB-tetracycline solution and tetracycline dissolved in ethanol, to achieve a final concentration of 5 μg/ml. The solution was then subjected to centrifugation twice (Beckman Coulter, JLA 10.5), combined with a mixture of 25 % polyethylene glycol (PEG) 6000 and 2.5 M NaCl (Sigma) and left to stir on ice for 90 min. After centrifugation, a white pellet was obtained, which was then resuspended in deionised water (DIW). This resuspended solution was deposited in 1.5 mL tubes and centrifuged in a microcentrifuge (SciSpin MICRO). The supernatant was transferred to new microcentrifuge tubes, PEG + NaCl was added, and the mixture was left on ice for 60 min. A final microcentrifuge step was performed, resulting in a white pellet of M13, which was resuspended in DIW.

2.2. Ultraviolet-Visible (UV–Vis) spectroscopy

The concentration of M13 in DIW was determined using an Aligent Cary 60 UV–Vis spectrophotometer with a 1 cm light path quartz cuvette. To establish a baseline, a spectrum of DIW was initially obtained. Prior to analysing the samples, they were transferred into 1.5 mL centrifuge tubes and placed on an orbital shaker for 1 min to ensure the uniform distribution of M13 in DIW. The concentration of M13 was then calculated based on the resulting spectrum using the Beer-Lambert Law, with an extinction coefficient of 3.84cm^2/mg at 269 nm. To confirm the viability of the M13 bacteriophage, specific characteristics in the spectrum were assessed. These included an absorbance peak at 269 nm (A_{269}), a local minimum absorbance at 245 nm (A_{245}), and a baseline at 350 nm (A_{350}). The purity and viability of the produced phages were determined based on the A_{269}/A_{245} ratio (~1.37) and the A_{350}/A_{269} ratio (~0.02) [41].

2.3. Fabrication of GraPhage13 aerogels (GPA)

The process of fabricating GraPhage13 aerogels (GPAs) has been adopted from Passaretti *et* al. [9], where the M13 and GO (Graphene Supermarket, SKU-HCGO-W-175ML) were added a 10 mM citrate buffer pH 4.9, to a final concentration of 0.3 mg/ml. This enabled the M13 and GO to self-assemble, forming an aggregate [10]. After thoroughly mixing the solution with an orbital shaker at 250 rpm for 15 min, it was centrifuged at 15,000 rpm for 1 min to produce a GO-M13 pellet. Removing 90 % of the supernatant and resuspending the pellet in the remaining supernatant generated the GraPhage13 hydrogel (GPH). Following this, 20 μL of GPH was deposited onto a 0.5 × 0.5 cm^2 silicon substrate and dried in a vacuum for 30 min, producing GPA. The fabricated GPAs were subsequently annealed (GenLab) between 50 and 250 °C for 30 min.

2.4. Scanning electron microscopy and pore size analysis

GPA morphology was imaged using a Hitachi SU5000 scanning electron microscope (SEM). To mitigate charging effects caused by the

insulating nature of GPAs, low-voltage imaging at 0.5 kV was employed. This approach was preferred to avoid obscuring pores with gold coating and preventing potential sample damage from high-energy electron beams. For the analysis of pore size distribution, ImageJ was utilized. [42]. The pixel size was converted to μm and to reduce noise and artefacts, which might be misinterpreted as pores, a Gaussian Blur filter was applied to the images for smoothing. Subsequently, the contrast was enhanced to improve pore visibility and a threshold was applied to generate a binary image. The separation of individual pores was achieved through a two-step dilation followed by a two-step erosion process. This allowed for precise pore area determination, facilitating the calculation of pore diameters and obtaining the pore size distribution.

2.5. Energy-Dispersive X-ray (EDX) spectroscopy

The elemental composition was determined *via* energy-dispersive X-ray spectroscopy using a Hitachi TM3030 microscope equipped with Oxford Instruments Swift ID, operating at 15 kV.

2.6. Force-Distance (F-D) curves

Force-distance curves were acquired using a Bruker Innova atomic force microscope equipped with Bruker DNP-10 probes. These probes consist of silicon nitride cantilevers with 20 nm silicon nitride tips, with a resonance frequency of 65 KHz and spring constant of 0.35 N/m.

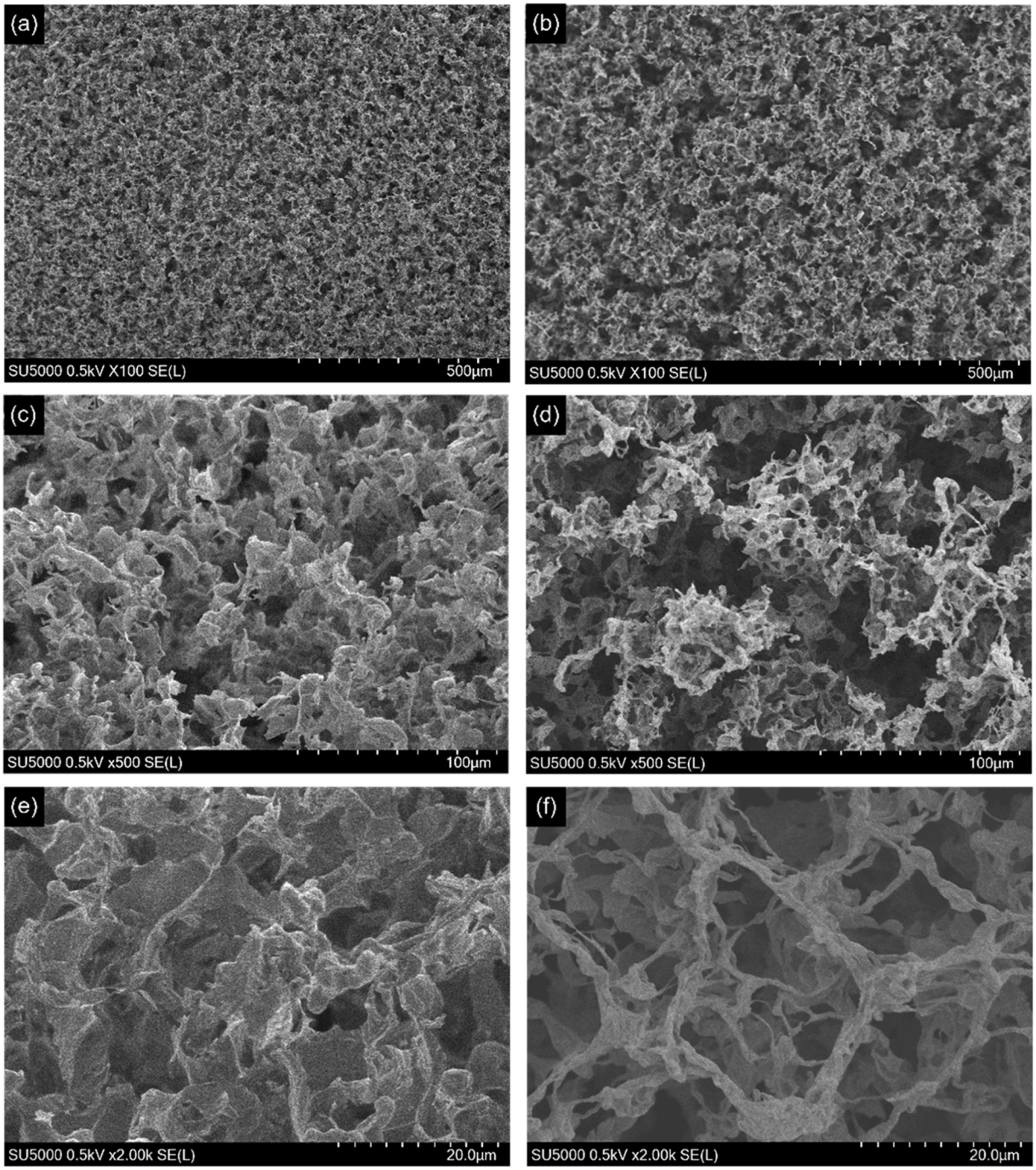

Fig. 1. Characteristic SEM images of micronano morphology at (a-b) 100x, (c-d) 500x and (e-f) 2000x magnifications of (a. c. e) GPA and of (b, f, f) GPA_{250}.

2.7. Raman spectroscopy with in-situ annealing

Raman microscope (Renishaw *inVia* Reflex Spectrometer System) was calibrated using Silicon with peak at 520 cm^{-1} [43]. The sample was then placed in the heating chamber, inserted into the chamber of Raman microscope, and connected to a temperature controller (Linkam Scientific Instruments Ltd TMS 94). Through initial investigations, it was found that the optimal laser wavelength to reduce damage to GPA was 442 nm at 0.5 % laser power, with an exposure time of 120 s to reduce the fluorescent background. The temperature varied between 25 °C and 300 °C at a heating rate of 10 °C/min and spectra were acquired at various increments. Subsequently, the spectra were processed using Origin Pro-through subtracting the baseline and fitting Lorentzian peaks to each spectrum.

3. Results and discussion

3.1. Micronano-morphology and composition

The morphology of GPA at ambient temperature was compared to GPA annealed at 250 °C for 30 min (GPA_{250}) (Fig. 1a-d). The specific GPAs were selected for comparison since they represent the two extremes of the attainable temperature range. The annealing process has been identified to cause irreversible changes to the micronano-structure of the nanocomposite (Fig. 1, c-d), with the original porous structure remaining intact even at the higher temperature of 250 °C. This is most probably due to the strong interactions between the positively charged N-terminus and K_8 residue of M13 and the carboxylic acid groups in GO [10]. These interactions increase its overall structural stability following annealing and consequently, prevent structural changes in the subsequent heating to similar temperatures.

Although the morphologies of GPA and GPA_{250} appear similar, there is a difference in the porosity, with the larger pore sizes identified for GPA_{250} compared to GPA. Accurately quantifying the change in pore size caused by the heat treatment poses significant challenges. Conventional methods such as gas sorption *e.g.,* BET, are generally used to detect pore sizes in the range of 2–50 nm [44], however SEM imaging reveals that pore size distribution present in the GPA are both <2 nm as well as >50 nm (Fig. 1). Furthermore, the combination of the mass requirements for BET measurements and the low density of GPAs complicates the generation of sufficient quantity for analysis [9,45]. An additional technique to ascertain the pore size distribution, *i.e.,* mercury porosimetry, entails the application of high-pressure gas, which warps the pore structure or destroys the aerogel. Furthermore, results obtained from BET and mercury poroismetry often exhibit significant discrepancies from each other and from the corresponding SEM images [46]. Considering the overall limitations, the in-depth analysis *via* SEM imaging enables the comparison of the average 2D pore size distribution (Fig. 2).

In Fig. 2, the variation in pore size distribution from SEM images ($n = 3$) taken over the same area highlights the differences between GPA and GPA_{250}. GPA is found to exhibit a notably higher number (1160 ± 40) of pores with diameter below 30 μm compared to the GPA_{250} (900 ± 30)). With the increase in the pore size, the distributions equalize, where both GPA and GPA_{250} exhibit a similar number of pores with diameters in the range of 40–50 μm. For diameters exceeding 50 μm, GPA_{250} exhibits a higher pore count (32 ± 4) compared to GPA (18 ± 3). This may be attributed to elevated temperatures, which lead to the removal of certain OCGFs through the emission of gases, such as the CO_2, disrupting bonds between GO and M13 and increasing the occurrence of larger pores [47,48].

The effect of temperature on the GPA was further investigated using energy dispersive x-ray (EDX) spectroscopy. The representative spectrum of GPA_{250}, (Fig. 3a) in comparison to the EDX spectra of GPA reported by Passaretti *et* al. and Stokes *et* al. [9,10], demonstrated a higher ratio of carbon-to-oxygen (C:O) for GPA_{250} relative to GPA. With the increase in annealing temperature from 25 °C to 250 °C, the C:O ratio is found to increase from 1.19 ± 0.01 for GPA to 1.58 ± 0.03 for GPA_{250} (Fig. 3b). This confirms that the higher annealing temperatures progressively reduce GO towards its reduced graphene oxide (rGO) form by removing its OCFGs, leading to an increase in the C:O ratio [49]. The reduction of GO, in turn, improves both the mechanical and electrical properties of GPA, highly applicable for the emerging miniaturised devices under development [50–52],

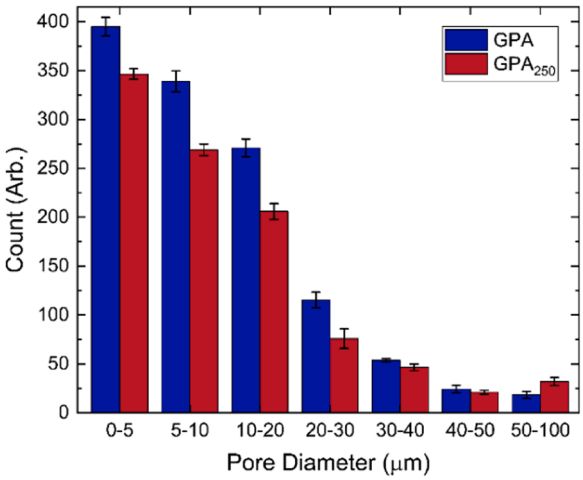

Fig. 2. The distribution of pore diameter of GPA and GPA_{250}. The count represents the number of pores detected in a SEM image at 100x magnification.

3.2. Nanomechanics

The nanomechanics of GPA annealed at varying temperatures has been subsequently investigated through the force-distance (F-D) curves (Fig. 4) obtained *via* AFM, allowing for a detailed examination of the mechanical response of GPA after being subjected to a range of annealing temperatures. This also provides further insights into the adhesion forces and stiffness of GPA, offering a comprehensive understanding of how this nanomaterial responds to temperature-induced changes.

Following the approach curves from right to left hand side shows an initial absence of contact between GPA and the tip results in zero force (Fig. 4). Once the attractive forces between the tip and GPA overcome the spring constant of the cantilever, the tip snaps into contact with the surface of GPA, leading to an observed increase in the force in the negative direction [53]. The tip continues the approach, indenting the GPA and bending the cantilever whilst increasing its deflection, until a set maximum force is obtained. Since the cantilever deflection is proportional to the force applied to the sample, the stiffness can be determined by calculating the force applied to GPA over the indentation distance. The stiffness quantifies the capacity of the sample to withstand external forces without undergoing deformation and can be derived by determining the gradient of the approach curve in the contact region, *i.e.,* above 0nN [54,55]. The variation in GPA stiffness *versus* varying temperatures is shown in Fig. 5a, where it is evident that the stiffness of GPA decreases with temperature, from 82.9 ± 0.6 N/m at 25 °C to 36.1 ± 0.4 N/m at 250 °C, most likely due the morphology. Shown in Figs. 1-3, subjecting GPA to higher temperatures increases the distance between surface asperities due to the removal of OCFGs, reducing the stress transfer through the structure, and therefore reducing the stiffness [56,57]. The decreasing strain with temperature could be also attributed to the crystal defects introduced into the GPA, inducing irregularities in its structure [58].

Subsequently, following the retraction curve (Fig. 4) from left to right, various attractive forces between the tip and the GPA, *e.g.,* electrostatic, capillary, van der Waals and contact forces, cause the tip to

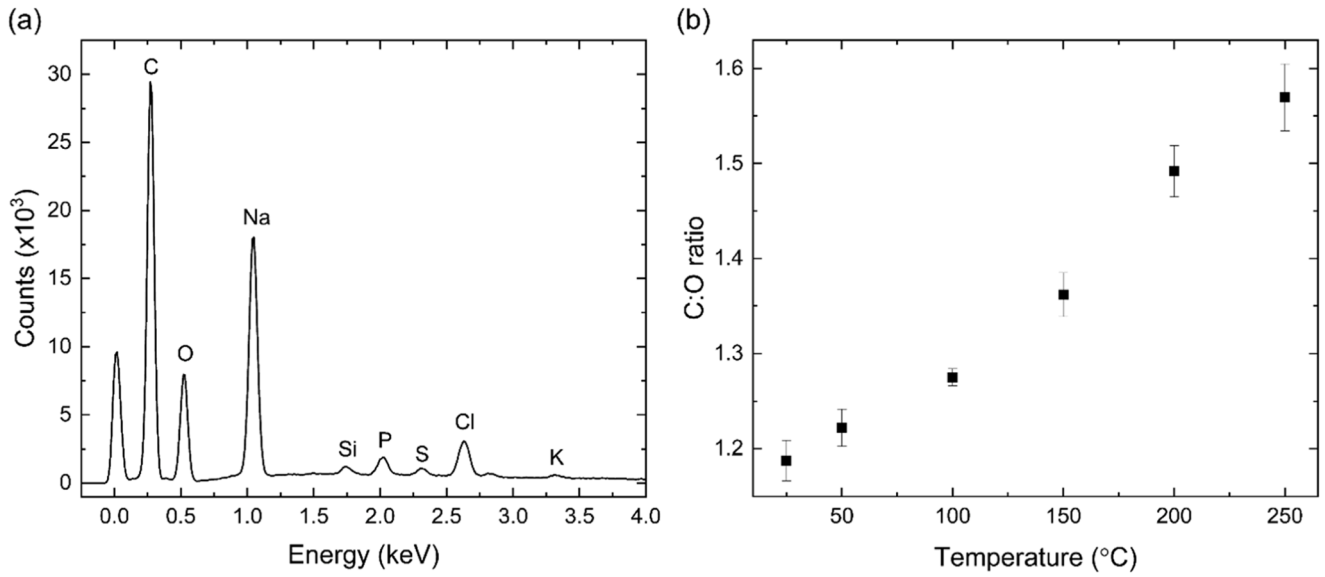

Fig. 3. (a). Representative EDX spectrum of GPA_{250}. (b). Change in carbon-to-oxygen ratio of GPA *versus* temperature.

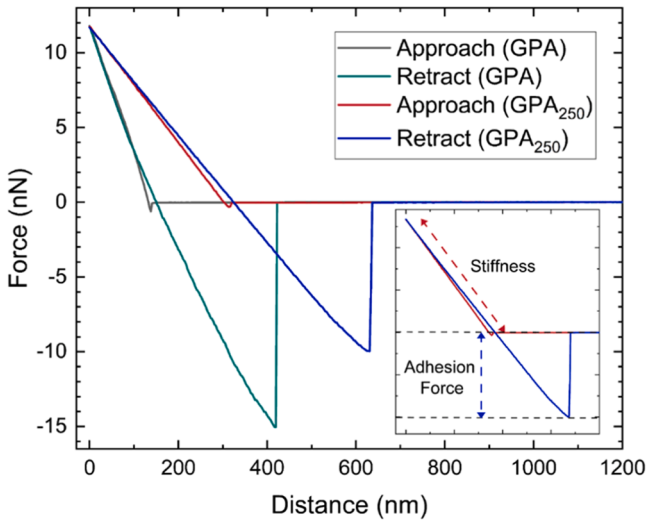

Fig. 4. Force-distance (F-D) curves for GPA and GPA_{250} obtained through atomic force microscopy. Inset: the stiffness is the gradient of the approach curve in the contact region and the adhesion force is the maximum negative force on the retraction curve.

bend towards and adhere to the sample as the tip retracts. The spring constant of the cantilever eventually overcomes the adhesion between the tip and GPA and disengages from the nanocomposite surface, restoring the force to zero. The adhesion force between the AFM probe and GPA is determined by the maximum negative force on the deflection curve [59,60].

The adhesion forces between the probe and GPAs annealed at different temperatures (Fig. 5b) indicate that increasing the annealing temperature results in the reduction of the adhesion force from 16.8 ± 0.1nN at 25 °C to 10.4 ± 0.6nN at 250 °C. This is attributed to structural changes to GPA. The F-D curves were conducted under ambient conditions, with forces arising from the capillary condensation dominating the adhesive forces [61,62]. Annealing GO leads to its gradual reduction towards the rGO, characterised by fewer OCFGs and more sp^2-hybridised carbon [49,63]. Since OCFGs interact with water whilst sp^2-hybridised carbon is hydrophobic, the reduction of GO leads to an increased hydrophobicity [64,65]. Water droplets on the surface of more hydrophobic structures demonstrate larger contact angles and high motilities, leading to a lower adhesion force [66,67].

Furthermore, the reduction in adhesion force may also relate to alterations in the porous micronano-morphology. Subjecting GPA to increased temperatures (Figs. 1-2) changes to pore size distribution, reducing the number of pores between 0 and 40 μm and increasing the number of pores in the range of 50–100 μm. Given that the adhesion force is related to the contact area between surface asperities, larger pore sizes result in a smaller contact area, reducing the adhesion force [68]. A reduction in the adhesion force also lowers the strain transfer between materials with a thermal expansion coefficient mismatch, such as GPA and the substrate or applied coatings. The ability of GPA to mitigate strain transfer under varying temperatures could lead to an improvement in stability and performance of future GPA-based devices [69,70].

3.3. *Raman spectroscopy with in-situ thermal treatment*

Raman spectroscopy was applied to study the changes to the structure of GPA and GPA_{250} with temperature. The *in-situ* thermal treatment setup enabled temperatures up to 300 °C to be accomplished. The representative spectra exhibit two prominent peaks at shifts of 1360 cm^{-1} and 1590 cm^{-1}, and signal-to-noise (SNR) ratio noticeably higher for GPA_{250} compared to GPA for the same acquisition time (Fig. 6a-b). This is attributed to several factors, including the temperature increase, which causes the water absorbed within the GPA to evaporate and subsequently condense on the walls of the heating chamber. Consequently, the laser focus is compromised, leading to a reduction in the number of counts and affecting the SNR. Furthermore, the spectra are affected by thermal background radiation. While the constant component of this radiation can be removed, random thermal fluctuations remain unaccounted for, leading to a decrease in the SNR [71].

The two characteristic peaks identified *via* Raman spectra for GPA and GPA_{250} could potentially be a superposition of multiple spectral bands. Therefore, to determine the optimal peak fitting, various fits were investigated for GPA and GPA_{250} (Fig,6, c-f) *via* the Bayesian Information Criterion (BIC), enabling a statistical comparison, with the fit with the lowest BIC value considered the most suitable for the spectrum analysis [16,72].

BIC values for Raman spectra of GPA fitted with varying numbers of peaks (Table 1) show a decrease of 974 from a 2-peak to a 4-peak fit, followed by a subsequent increase of 20 for a 5-peak fit, indicating that

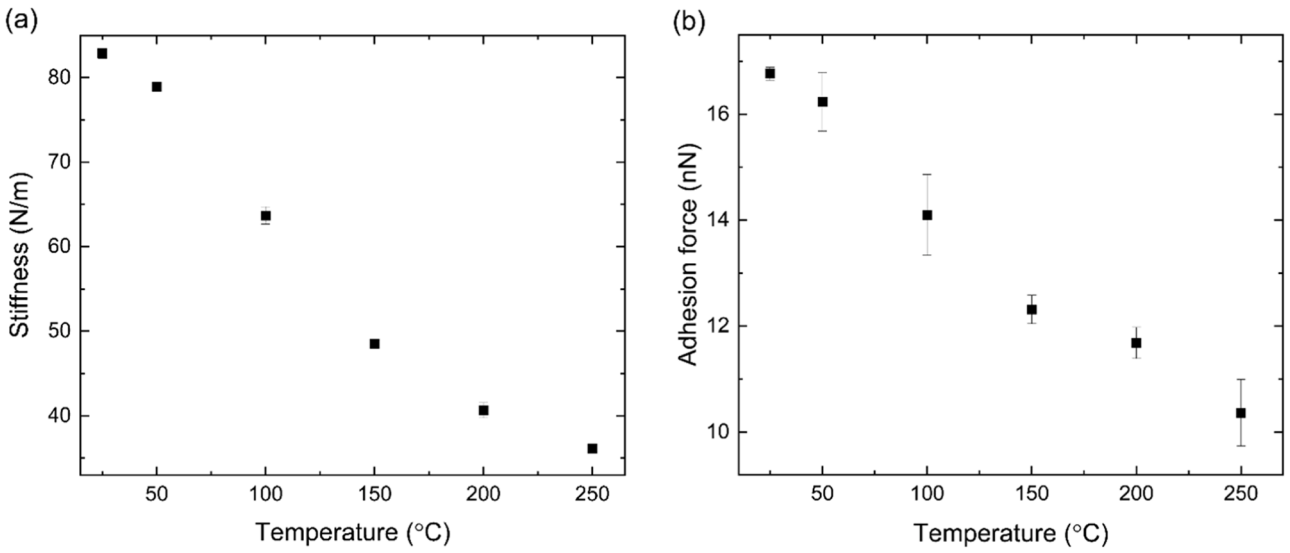

Fig. 5. The change in (a) stiffness of GPA and (b) the adhesion force between the AFM probe and the GPA, with increasing annealing temperature.

the 4-peak fit (Fig. 6e) is the optimal choice. The G-mode peak (Figs. 6, c-f) arises from the stretching of the sp^2 bonds between pairs of carbon atoms, whilst the D'-mode is attributed to crystal defects, which stem from the functionalisation of sp^2 bonds in GO, resulting in a disorder-induced phonon mode [73,74]. The G^- mode originates from the presence of defects from amorphous sp^2 bonded structures, resulting from the softening of carbon-carbon bonds due to the functionalisation of GO [74]. This has previously been associated with the presence of M13 disrupting the graphene plane, or charge transfer between M13 and GO [16]. The peak profile over the D-mode range likely has a contribution from both sp^2 and sp^3 peaks. In graphene-based materials, the D-band is often associated with the presence of defects, edges, or other structural disorders, therefore sp^2 hybridised carbon atoms in the graphene lattice can contribute to the D-band, especially if there are defects or irregularities in the hexagonal structure. Additionally, the sp^3 hybridised carbon atoms, which are characteristic of amorphous carbon or carbon with a more disordered structure, can also contribute to the D-band [9, 16,75].

Conversely, for GPA_{250}, the 2-peak fit exhibits the lowest BIC value (Fig. 6d), suggesting it is the most suitable peak fit instead of the 4-peak fit (Fig. 6f). The difference in the optimal fitting between GPA and GPA_{250} can be attributed to structural changed induced by the different temperatures. The D′ peak tends to merge with the G peak at high defect concentrations, suggesting that exposing GPA to elevated temperatures leads to an increase in the number of defects within the structure [76]. However, it should be noted that the G^-, G and D' peaks in the 4-peak fit are all associated with the presence of sp^2 bonds and can be superimposed to form the G-mode peak in the 2-peak fit. Therefore, for the purpose of tracking the effect of temperature on the Raman spectrum, the two-peak fit with the D-mode and G-mode is sufficient. The two-peak fit for GPA and GPA_{250} is shown in Fig. 6c and d, respectively.

Fig. 7 illustrates the position of the D and G peaks as the temperature is incrementally increased *in-situ* within Raman spectrometer. This was compared to the predicted trend of the shift caused by the thermal expansion of graphite, GO and diamond, derived by comparing the thermal expansion to the relationship between strain and Raman shift, to determine whether changes in the position of D and G modes are a consequence of thermal expansion of GPA [77–80]. The thermal expansion of a material results from the response of its structure and bonds to changes in temperature. By comparing the temperature-dependent evolution of the Raman D band frequency of diamond, a sp^3 hybridised structure, to that of GPA, allows to discern whether the D peak is predominantly influenced by sp^3 bonds. This would exhibit a downward shift with an increase in temperature. Conversely, if it is influenced by sp^2 bonds, it would demonstrate an upward shift, consistent with a small yet negative thermal expansion coefficient of graphene and in-plane graphite, leading to the stiffening of sp^2 carbon-carbon bonds. Conversely, the G peak represents the sp^2 bonds in GPA, capturing the functionalisation and defects associated with these bonds. However, unlike its constituent GO, exhibits a three-dimensional carbon-based architecture and therefore, the Raman shift caused by the thermal expansion of both GO and graphite was compared to the Raman shift of the G peak [81,82].

The general trend in Fig. 7a demonstrates that the D peak position decreases as the temperature increases, with the largest Raman shift of 1369.1 ± 0.7 cm^{-1} at 40 °C and the lowest of 1363 ± 3 cm^{-1} at 300 °C. This redshift with temperature suggests the softening of the carbon-carbon bonds, with the predominant influence being attributed to the sp^3 Raman mode rather than the predicted sp^2 D-mode [81]. On the other hand, the position of the G peak progressively increases with temperature (Fig. 7b) [16], exhibiting a minimum shift of 1586.5 ± 0.4 cm^{-1} at 25 °C and reaching 1592 ± 2 cm^{-1} at 300 °C, demonstrating the stiffening of sp^2 bonds and therefore implying that both the stiffening and softening of carbon-carbon bonds occur in GPA, demonstrating the different inherent structures present. Further, the predicted Raman shift for diamond with the D-mode (Fig. 7a) demonstrates downshift with temperature, indicating that the position of the latter is dependent on the thermal expansion of GPA. Moreover, Fig. 7a demonstrates that the thermal expansion rate of sp^3 bonds in GPA exceeds that of the crystalline sp^3 structure, revealing a distinctive thermal behaviour. The difference in the thermal expansion rates, with the D-mode showing a downshift of 0.030 ± 0.003 $cm^{-1}/°C$ and diamond a downshift of 0.0093 $cm^{-1}/°C$, could be because of the differences in the microstructure of GPA and diamond. However, it could also be indicative of presence of defects in the GPA micronano-structure, increasing the distance between neighbouring carbon atoms [81].

Furthermore, comparing the temperature-induced upshift of the GPA G-mode with the thermal expansion of graphite and GO (Fib. 7b) reveals the in-plane thermal expansion of GPA between graphite and GO. The substantial deviation in the Raman shift trend, in contrast to the thermal contraction behaviour of GO, suggests that the in-plane thermal expansion of GO in GPA is not solely influenced by thermal contraction of the sp^2 bonds, but also by the GPA micronano-structure. The larger shift rates for the GPA G-mode compared to the graphite in-plane thermal expansion demonstrate complex in-plane thermal expansion of the nanocomposite, determined by the functionalisation of GO. The

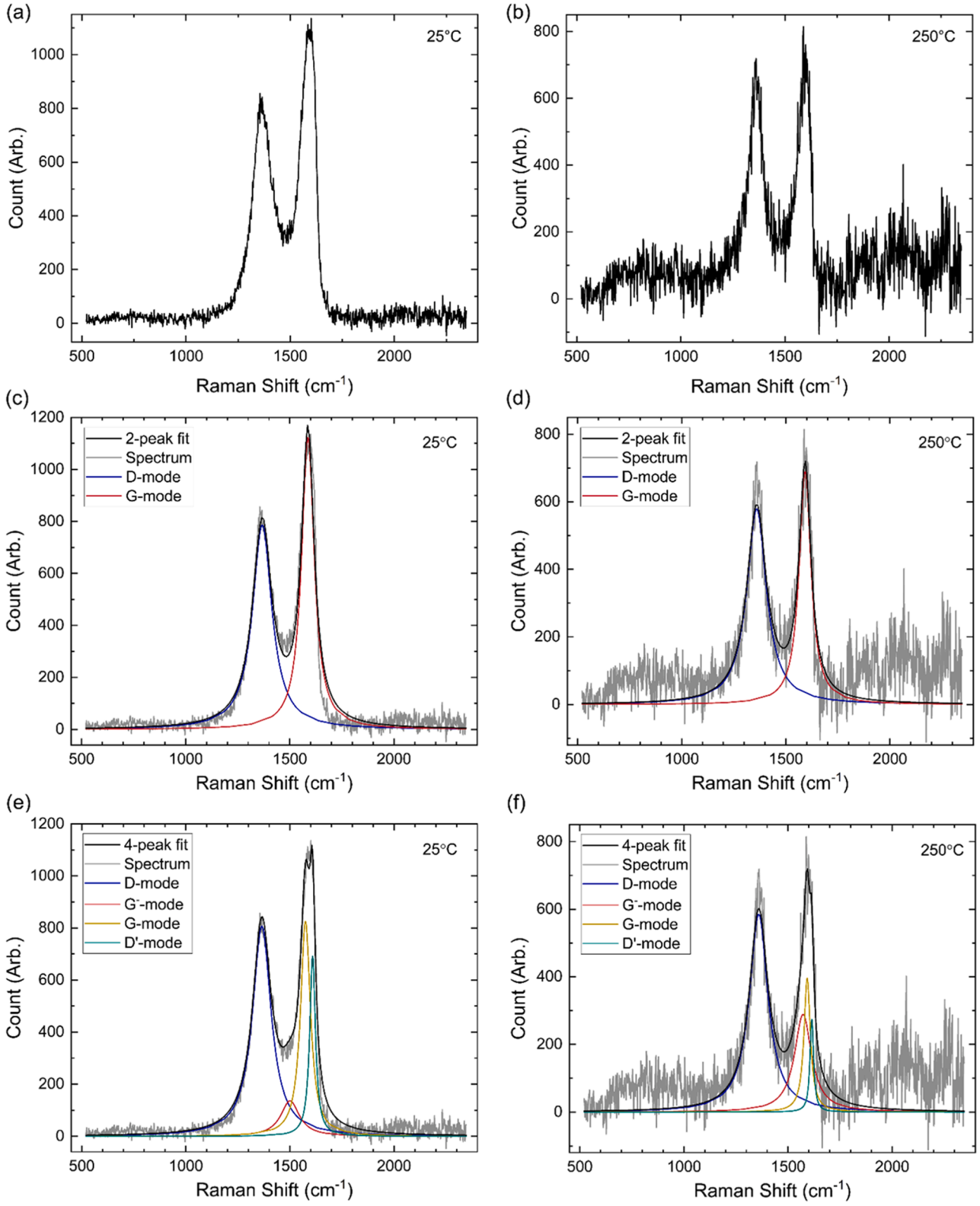

Fig. 6. Raman spectra of (a) GPA and (b) GPA_{250} with the optimal 2-peak fit (c-d) and 4-peak fit (e-f), respectively.

upshift in the G-mode, lying between the thermal expansion of graphite and GO, indicates that the functionalisation of GPA does impact the thermal expansion coefficient of the sp^2 C-C bonds, highlighting a unique nanomechanical feature in the nanocomposite [79,83].

To explore further potential indicators for structural changes of GPA with temperature, the relationship between the temperature and the full width half maximum (FWHM) of the Raman peaks was analysed. Both the D-mode (Fig. 8a) and the G-mode (Fig. 8b) FWHM are found to decrease with temperature from 25 °C to 200 °C, with the D-mode decreasing from 114 ± 2 cm^{-1} to 82 ± 2 cm^{-1} and the G-mode from 74 ± 1 cm^{-1} to 61 ± 2 cm^{-1}. This represents the gradual reduction of GO whilst some of the OCFGs are removed [84,85]. Beyond the temperature

Table 1
Comparison of the BIC values of the 2-peak and 4-peak fits to the Raman spectra of GPA acquired at 25 °C and 250 °C.

Sample	BIC Value			
	2-peak	3-peak	4-peak	5-peak
GPA	7665	7073	6691	6711
GPA_{250}	9186	9190	9202	9223

of 200 °C, there is a general increase in the FWHM, with the G-mode increasing to 104 ± 6 cm^{-1} at 300 °C and the D-mode increasing to 131 ± 6 cm^{-1} at 270 °C. The significant change in the FWHM observed at temperatures higher than 200 °C demonstrates the increase in structural deformation [86]. This corresponds with the observations in SEM images (Fig. 1) of the structural changes caused by high temperature treatment. Moreover, this is consistent with Fig. 5a, illustrating a decrease in GPA stiffness with increasing temperature thereby, rendering the GPA more prone to deformation.

To further understand the reduction in the D-mode FWHM to 90 ± 8 cm^{-1} at 300 °C and investigate the temperature-induced alterations in the micronano-structure of GPA, the ratio of the D-mode and G-mode intensities (I_D/I_G) was examined (Fig. 9), which provides a measure of defects in GPA with temperature [84]. Between 25 °C and 60 °C, I_D/I_G decreases from 1.07±0.02 to 0.90 ± 0.02, whereafter, the I_D/I_G increases with temperature to 1.3 ± 0.1 at 270 °C until a sudden drop-off at 300 °C, which has an I_D/I_G value of 0.57 ± 0.04, closely resembling previous findings of I_D/I_G for GO [87,88].

There are two competing mechanisms contributing towards the I_D/I_G ratio with increase in temperature. As GO decomposes, OCFGs are removed from the structure, reducing the number of defects and therefore, lowering the I_D/I_G. However, some of the OCFGs removed may be carbonyl and carboxyl groups, and carbon atoms are removed from the structure through the elimination of these functional groups, in the form of gases such as CO and CO_2. This generates crystal defects in GPA and therefore increases I_D/I_G [48,89,90]. GO starts to decompose at temperatures above 60 °C, however, a decrease in I_D/I_G is visible below this temperature.

This can be attributed to the desorption of water within the GPA structure, which reduces the number of defects. The increase in I_D/I_G

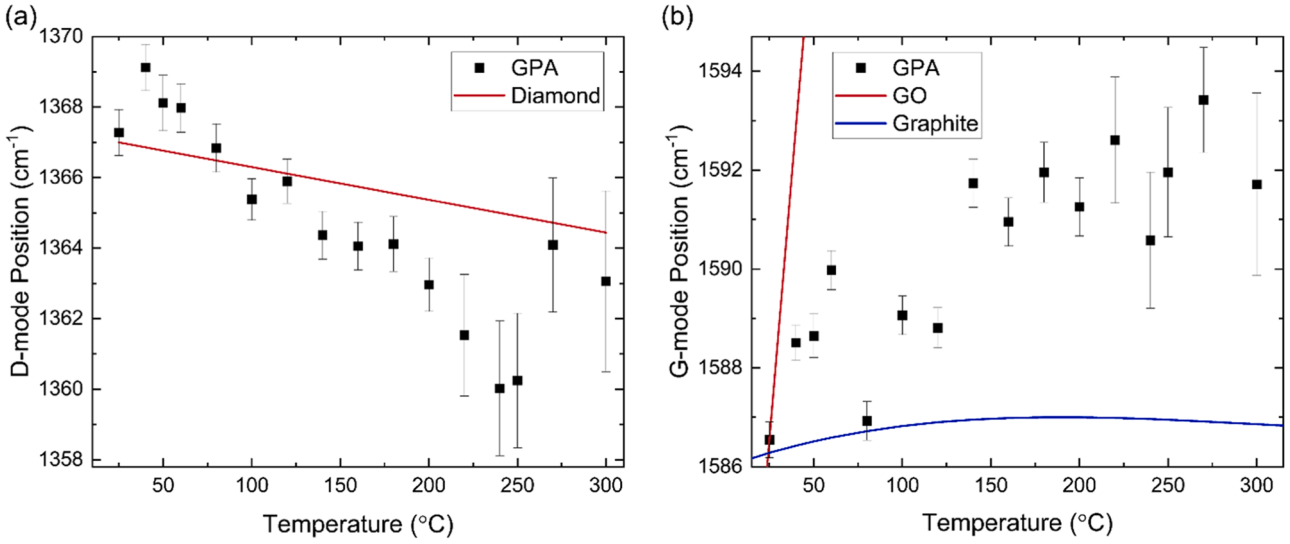

Fig. 7. Position of Raman peaks for GraPhage13 aerogels with temperature: (a) Position of D-mode compared to the Raman shift resulting from thermal expansion of diamond and (b) position of the Raman shift resulting from thermal expansion of graphene oxide and graphite.

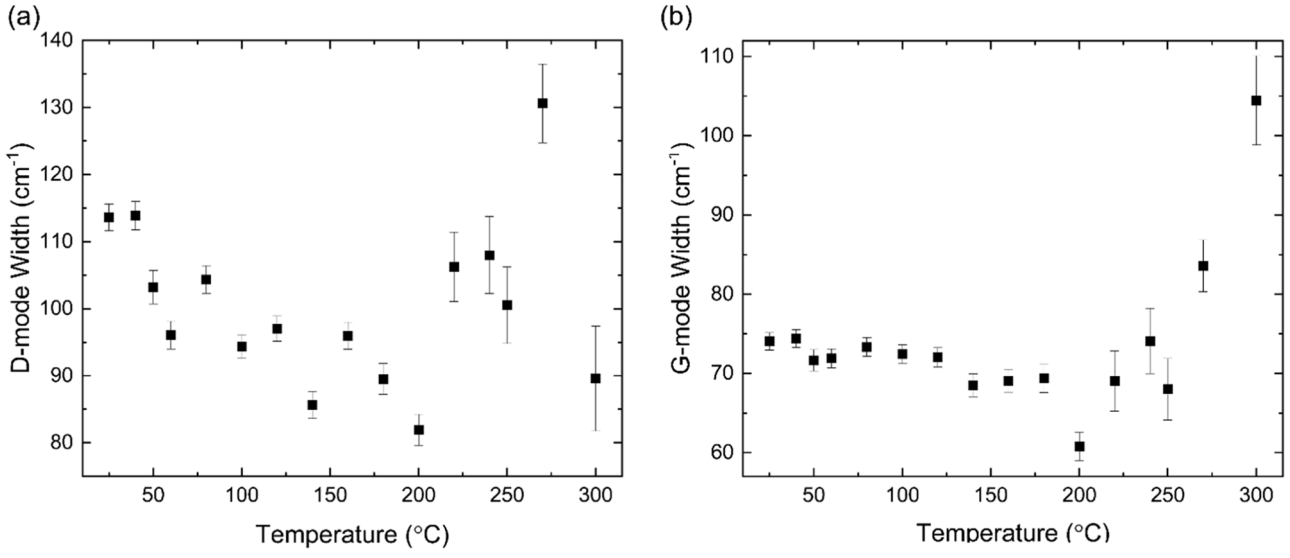

Fig. 8. The full width half maximum (FWHM) of the GPA (a) D-mode and (b) G-mode Raman peaks as function of temperature.

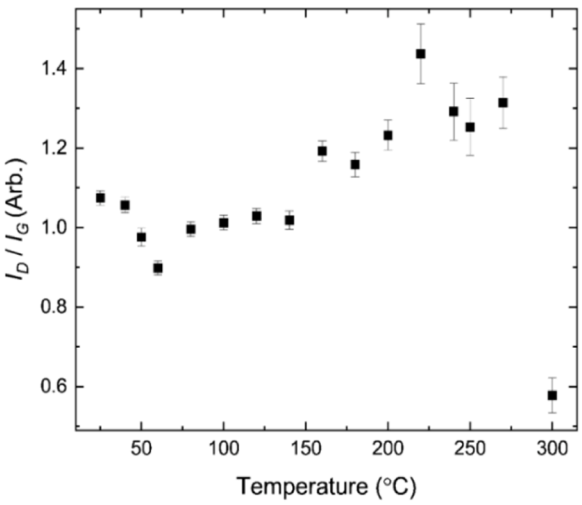

Fig. 9. The D-mode/G-mode intensity ratio (I_D/I_G) for GPA *versus* temperature.

between 60 °C and 270 °C suggests the increased removal of carboxyl and carbonyl groups with temperature. The sudden decrease in I_D/I_G at 300 °C implies that further OCFGs are being removed without the additional carbon atoms and since the epoxy groups are removed at temperatures higher than 400 °C, it is likely that the decrease in I_D/I_G signifies the onset of the hydroxyl groups removal from GO [49,85,86].

4. Conclusions

The effect of annealing GraPhage13 aerogels (GPA) on their micronano-morphology, composition and nanomechanical properties has been investigated through a suite of SEM, EDX, AFM force measurements and Raman spectrometry. The EDX spectra revealed that annealing GPA increases the carbon-to-oxygen ratio, with the gradual reduction of graphene oxide (GO) through the elimination of its oxygen-containing functional groups (OCFGs). The occurrence of crystal defects in GPA with temperature was also found to depend on the elimination of OCFGs and consequently, the removal of the carbon attached to the carbonyl and carboxyl groups. Annealing GPA also changes its nanomechanical properties, with both the adhesion force between the AFM probe and the GPA as well as the stiffness of the nanocomposite decreasing with an increase in temperature.

The structural changes of GPA with temperature ranging from 25 °C to 300 °C have been further studied *via* Raman spectroscopy with an *in-situ* annealing. The representative spectra of GPA demonstrated two dominant peaks, with the D-mode arising from contribution of sp^3 Raman peak and the peak originating from disordered sp^2 carbon, and the G-mode from the stretching of sp^2 carbon-carbon bonds. The D-mode was found to downshift with the increase in temperature, attributed to the softening of sp^3 bonds and the presence of defects. Conversely, the G-mode was found to upshift, owing to the stiffening of sp^2 bonds due to the negative thermal expansion coefficient of GO. Comparing the D-mode and G-mode Raman shift to the thermal expansion of diamond, GO and graphite demonstrated the unique thermal and nanomechanical behaviours of GPA. The thermal expansion rate of sp^3 bonds in GPA surpasses that observed in a crystalline sp^3 structure and the sp^2 bonds in GPA exhibit a thermal expansion between graphite and GO, indicating that the functionalisation of GO influences the thermal expansion of GPA. GraPhage13 aerogel, derived from the self-assembly of graphene oxide and M13 bacteriophage, presents a micro-porous structure with potential industrial applications. Annealing at elevated temperatures results in the removal of oxygen-containing functional groups from GPA, transforming GO into reduced graphene oxide, and leading to larger pore sizes, smaller contact areas and hen\ce reduced adhesion and stiffness. Notably, GPA exhibits unique thermal behaviours where the sp3 bonds expand more than in crystalline structures, and sp2 bonds contract in a range intermediate between graphite and GO. These findings highlight the significant influence of GO functionalization on GPA's thermal properties. Advanced Raman spectroscopy analysis further reveals consistent defect levels and exceptional thermal-mechanical stability at the nanoscale. The enhanced understanding of GPA's properties post-annealing indicates its applicability in diverse areas including electronic and photonic devices, energy storage and conversion systems, environmental applications, and smart material systems.

Overall, this study demonstrates the effect of temperature on the micronano-composition and nanomechanics of GPA as well as providing the underpinning insights into the mechanism behind these changes, whilst yielding the temperature-dependent properties and *tunability* of GPA and thus, laying the platform towards its exploitation in a range of applications as a versatile material in carbon-based technology. For instance, the tuneable nanomechanical properties of the GPA make it a promising candidate for the development of advanced sensors, capable of detecting subtle environmental changes, whereas its enhanced stability and performance within a broad range of temperatures, indicate its potential as a reliable material for energy storage systems, where thermal fluctuations are common. The overall unveiled unique characteristic of this nanocomposite paves the way for the design and implementation of GPA in miniaturised devices, showcasing its versatility and importance in advancing technological innovations.

CRediT authorship contribution statement

Kate Stokes: Writing – review & editing, Writing – original draft, Methodology, Investigation. **Yiwei Sun:** Writing – review & editing, Writing – original draft, Supervision, Methodology, Data curation. **Haowei Zhang:** Writing – original draft, Methodology, Investigation. **Paolo Passaretti:** Methodology, Investigation. **Henry White:** Resources, Project administration. **Pola Goldberg Oppeneheimer:** Writing – original draft, Visualization, Validation, Supervision, Resources, Project administration, Methodology, Investigation, Funding acquisition, Formal analysis, Data curation, Conceptualization.

Declaration of competing interest

The authors declare that they have no known competing financial interests or personal relationships that could have appeared to influence the work reported in this paper.

Data availability

Data will be made available on request.

Acknowledgments

We acknowledge the BAE Systems (BS/1464085) and the EPSRC Centre for Doctoral Training in Formulation Engineering (EP/S023070/1). We also acknowledge funding by the EPSRC (EP/V029983/1 and EP/W004593/1) and the Wellcome Trust (174ISSFPP).

References

[1] S.C. Ray, Application and uses of graphene oxide and reduced graphene oxide, in: S.C. Ray (Ed.), Applications of Graphene and Graphene-Oxide Based Nanomaterials, William Andrew Publishing, Oxford, 2015, pp. 39–55, ch. 2.
[2] P. Passaretti, Graphene Oxide and Biomolecules for the Production of Functional 3D Graphene-Based Materials, *Front. Mol. Biosci.*, Rev. 9 (2022), https://doi.org/10.3389/fmolb.2022.774097.
[3] A. Aidun, et al., Graphene oxide incorporated polycaprolactone/chitosan/collagen electrospun scaffold: enhanced osteogenic properties for bone tissue engineering, Artif. Organs 43 (10) (2019) E264–E281, https://doi.org/10.1111/aor.13474.

[4] J. Zhang, H. Eyisoylu, X.-H. Qin, M. Rubert, R. Müller, 3D bioprinting of graphene oxide-incorporated cell-laden bone mimicking scaffolds for promoting scaffold fidelity, osteogenic differentiation and mineralization, Acta Biomater. 121 (2021) 637–652, https://doi.org/10.1016/j.actbio.2020.12.026.

[5] C. Wen, X. Zhan, X. Huang, F. Xu, L. Luo, C. Xia, Characterization and corrosion properties of hydroxyapatite/graphene oxide bio-composite coating on magnesium alloy by one-step micro-arc oxidation method, Surf. Coat. Technol. 317 (2017) 125–133, https://doi.org/10.1016/j.surfcoat.2017.03.034.

[6] H. Wu, L. Cheng, C. Liu, X. Lan, H. Zhao, Engineering the interface in graphene oxide/epoxy composites using bio-based epoxy-graphene oxide nanomaterial to achieve superior anticorrosion performance, J. Colloid Interface Sci. 587 (2021) 755–766, https://doi.org/10.1016/j.jcis.2020.11.035.

[7] S. Javanbakht, M. Pooresmaeil, H. Namazi, Green one-pot synthesis of carboxymethylcellulose/Zn-based metal-organic framework/graphene oxide bio-nanocomposite as a nanocarrier for drug delivery system, Carbohydr. Polym. 208 (2019) 294–301, https://doi.org/10.1016/j.carbpol.2018.12.066.

[8] Z. Karimzadeh, S. Javanbakht, H. Namazi, Carboxymethylcellulose/MOF-5/Graphene oxide bio-nanocomposite as antibacterial drug nanocarrier agent, Bioimpacts. 9 (1) (2019) 5–13, https://doi.org/10.15171/bi.2019.02.

[9] P. Passaretti, et al., Multifunctional graphene oxide-bacteriophage based porous three-dimensional micro-nanocomposites, Nanoscale 11 (28) (2019) 13318–13329, https://doi.org/10.1039/C9NR03670A.

[10] K. Stokes, Y. Sun, P. Passaretti, H. White, P.G. Oppenheimer, Optimisation of GraPhage13 macro-dispersibility via understanding the pH-dependent ionisation during self-assembly: towards the manufacture of graphene-based nanodevices, Nanoscale 15 (2023) 13304–13312, https://doi.org/10.1039/d3nr00778b.

[11] I.W. Park, et al., Recent developments and prospects of M13- bacteriophage based piezoelectric energy harvesting devices, Nanomaterials. (Basel) 10 (1) (2020), https://doi.org/10.3390/nano10010093.

[12] P. Passaretti, I. Khan, T.R. Dafforn, P. Goldberg Oppenheimer, Improvements in the production of purified M13 bacteriophage bio-nanoparticle, Sci. Rep. 10 (1) (2020) 18538, https://doi.org/10.1038/s41598-020-75205-3.

[13] S.M. Lee, et al., Engineered M13 bacteriophage-enhanced colorimetric detection of allergenic fungi, Sens. Actuators B 393 (2023) 134244, https://doi.org/10.1016/j.snb.2023.134244.

[14] P. Wang, et al., A single thiolated-phage displayed nanobody-based biosensor for label-free detection of foodborne pathogen, J. Hazard. Mater. 443 (2023) 130157, https://doi.org/10.1016/j.jhazmat.2022.130157.

[15] H. Kim, et al., M13 Virus Triboelectricity and Energy Harvesting, Nano Lett. 21 (16) (2021) 6851–6858, https://doi.org/10.1021/acs.nanolett.1c01881.

[16] Y. Sun, et al., Nanomechanics of graphene oxide-bacteriophage based self-assembled porous composites, Sci. Rep. 10 (1) (2020) 15618, https://doi.org/10.1038/s41598-020-72372-1.

[17] Y. Qin, C. Xue, H. Yu, Y. Wen, L. Zhang, Y. Li, The construction of bio-inspired hierarchically porous graphene aerogel for efficiently organic pollutants absorption, J. Hazard. Mater. 419 (2021) 126441, https://doi.org/10.1016/j.jhazmat.2021.126441.

[18] J. Huang, D. Li, L. Huang, S. Tan, T. Liu, Bio-based aerogel based on bamboo, waste paper, and reduced graphene oxide for oil/water separation, Langmuir. 38 (10) (2022) 3064–3075, https://doi.org/10.1021/acs.langmuir.1c02821.

[19] R. Chen, X. Li, Q. Huang, H. Ling, Y. Yang, X. Wang, Self-assembled porous biomass carbon/RGO/nanocellulose hybrid aerogels for self-supporting supercapacitor electrodes, Chem. Eng. J. 412 (2021) 128755, https://doi.org/10.1016/j.cej.2021.128755.

[20] Y. Wang, J. Yang, Y. Song, Q. Yang, C. Xiong, Z. Shi, Porous and three-dimensional carbon aerogels from nanocellulose/pristine graphene for high-performance supercapacitor electrodes, Diam. Relat. Mater. 132 (2023) 109626, https://doi.org/10.1016/j.diamond.2022.109626.

[21] X. Yuan, Y. Wei, S. Chen, P. Wang, L. Liu, Bio-based graphene/sodium alginate aerogels for strain sensors, RSC Adv. 6 (68) (2016) 64056–64064, https://doi.org/10.1039/C6RA12469K.

[22] H. Liu, et al., Multifunctional superelastic, superhydrophilic, and ultralight nanocellulose-based composite carbon aerogels for compressive supercapacitor and strain sensor, Adv. Funct. Mater. 32 (26) (2022) 2113082, https://doi.org/10.1002/adfm.202113082.

[23] E.M. Lucas, M.S. Doescher, D.M. Ebenstein, K.J. Wahl, D.R. Rolison, Silica aerogels with enhanced durability, 30-nm mean pore-size, and improved immersibility in liquids, J. Non Cryst. Solids 350 (2004) 244–252, https://doi.org/10.1016/j.jnoncrysol.2004.07.074.

[24] T. Chen, et al., Temperature-adaptable pressure sensors based on MXene-coated GO hierarchical aerogels with superb detection capability, Carbon N Y 200 (2022) 47–55, https://doi.org/10.1016/j.carbon.2022.08.002.

[25] S.P. Patil, V.G. Parale, H.-H. Park, B. Markert, Molecular dynamics and experimental studies of nanoindentation on nanoporous silica aerogels, Mater. Sci. Eng. 742 (2019) 344–352, https://doi.org/10.1016/j.msea.2018.11.019.

[26] V. Ramasubbu, F.S. Omar, K. Ramesh, S. Ramesh, X.S. Shajan, Three-dimensional hierarchical nanostructured porous TiO2 aerogel/Cobalt based metal-organic framework (MOF) composite as an electrode material for supercapattery, J. Energy Storage 32 (2020) 101750, https://doi.org/10.1016/j.est.2020.101750.

[27] Y. Hanzawa, H. Hatori, N. Yoshizawa, Y. Yamada, Structural changes in carbon aerogels with high temperature treatment, Carbon N Y 40 (4) (2002) 575–581, https://doi.org/10.1016/S0008-6223(01)00150-6.

[28] M.M. Atta, E.O. Taha, A.M. Abdelreheem, Nitrogen plasma effect on the structural, thermal, and dynamic mechanical properties of PVA/starch/graphene oxide nanocomposite, Appl. Phys. A 127 (7) (2021) 532, https://doi.org/10.1007/s00339-021-04671-x.

[29] I. Sarbu, C. Sebarchievici, A comprehensive review of thermal energy storage, Sustainability. 10 (1) (2018) 191, https://doi.org/10.3390/su10010191.

[30] H. Zhang, J. Baeyens, G. Cáceres, J. Degrève, Y. Lv, Thermal energy storage: recent developments and practical aspects, Prog. Energy Combust. Sci. 53 (2016) 1–40, https://doi.org/10.1016/j.pecs.2015.10.003.

[31] J. Zhang, X. Liu, G. Neri, N. Pinna, Nanostructured materials for room-temperature gas sensors, Adv. Mater. 28 (5) (2016) 795–831, https://doi.org/10.1002/adma.201503825.

[32] W. Yan, et al., Conductometric gas sensing behavior of WS2 aerogel, FlatChem 5 (2017) 1–8, https://doi.org/10.1016/j.flatc.2017.08.003.

[33] X. Zhu, S. Li, Y. Shi, N. Cai, Recent advances in elevated-temperature pressure swing adsorption for carbon capture and hydrogen production, Prog. Energy Combust. Sci. 75 (2019) 100784, https://doi.org/10.1016/j.pecs.2019.100784.

[34] P. Priyadarshini, G. Rim, C. Rosu, M. Song, C.W. Jones, Direct air capture of CO2 using amine/alumina sorbents at cold temperature, ACS. Environ. Au 3 (5) (2023) 295–307, https://doi.org/10.1021/acsenvironau.3c00010.

[35] X. Huang, G. Yu, Y. Zhang, M. Zhang, G. Shao, Design of cellular structure of graphene aerogels for electromagnetic wave absorption, Chem. Eng. J. 426 (2021) 131894, https://doi.org/10.1016/j.cej.2021.131894.

[36] B. Zhao, et al., Lightweight graphene aerogels by decoration of 1D CoNi chains and CNTs to achieve ultra-wide microwave absorption, Carbon N Y 176 (2021) 411–420, https://doi.org/10.1016/j.carbon.2021.01.136.

[37] K. Ji, et al., A tunable amphiphilic Enteromorpha-modified graphene aerogel for oil/water separation, Sci. Total Environ. 763 (2021) 142958, https://doi.org/10.1016/j.scitotenv.2020.142958.

[38] Y. Mu, et al., Rapid and facile fabrication of hierarchically porous graphene aerogel for oil-water separation and piezoresistive sensing applications, Appl. Surf. Sci. 613 (2023) 155982, https://doi.org/10.1016/j.apsusc.2022.155982.

[39] T. Yan, et al., Ultrahigh-energy-density sorption thermal battery enabled by graphene aerogel-based composite sorbents for thermal energy harvesting from air, ACS. Energy Lett. 6 (5) (2021) 1795–1802, https://doi.org/10.1021/acsenergylett.1c00284.

[40] D. Wei, C. Wu, G. Jiang, X. Sheng, Y. Xie, Lignin-assisted construction of well-defined 3D graphene aerogel/PEG form-stable phase change composites towards efficient solar thermal energy storage, Solar Energy Mater. Solar Cells 224 (2021) 111013, https://doi.org/10.1016/j.solmat.2021.111013.

[41] O. Morag, N.G. Sgourakis, G. Abramov, A. Goldbourt, Filamentous bacteriophage viruses: preparation, magic-angle spinning solid-state NMR experiments, and structure determination, in: R. Ghose (Ed.), Protein NMR: Methods and Protocols, Springer New York, New York, NY, 2018, pp. 67–97.

[42] N. Hojat, P. Gentile, A.M. Ferreira, L. Šiller, Automatic pore size measurements from scanning electron microscopy images of porous scaffolds, J. Porous Mater. 30 (1) (2023) 93–101, https://doi.org/10.1007/s10934-022-01309-y.

[43] K. Uchinokura, T. Sekine, E. Matsuura, Raman scattering by silicon, Solid State Commun. 11 (1) (1972) 47–49, https://doi.org/10.1016/0038-1098(72)91127-1.

[44] P.S. Liu, G.F. Chen, Characterization methods: basic factors, in: P.S. Liu, G.F. Chen (Eds.), Porous Materials, Butterworth-Heinemann, Boston, 2014, pp. 411–492, ch. 9.

[45] E. Karg, G.A. Ferron, G. Schumann, O. Schmid, Specific BET Surface Area Measurement of Low-Mass-Samples, in: ETH Nanoparticles Conference, Switzerland, Zurich, 2008 [Online]. Available[Online]. Available, https://www.nanoparticles.ch/archive/2008_Karg_PR.pdf.

[46] G. Horvat, M. Pantić, Ž. Knez, Z. Novak, A Brief Evaluation of Pore Structure Determination for Bioaerogels, Gels. 8 (7) (2022), https://doi.org/10.3390/gels8070438.

[47] A.F. Betancur, A. García, F.R. Pérez, Thermal stability and chemical analysis of hybrid materials reinforced with graphene oxide, J. Phys. 1219 (1) (2019) 012003, https://doi.org/10.1088/1742-6596/1219/1/012003.

[48] C. Li, et al., Effect of long-term ageing on graphene oxide: structure and thermal decomposition, R. Soc. Open. Sci. 8 (12) (2021) 202309, https://doi.org/10.1098/rsos.202309.

[49] I. Sengupta, S. Chakraborty, M. Talukdar, S.K. Pal, S. Chakraborty, Thermal reduction of graphene oxide: how temperature influences purity, J. Mater. Res. 33 (23) (2018) 4113–4122, https://doi.org/10.1557/jmr.2018.338.

[50] E. Jaafar and M. Kashif, *Study on Morphological, Optical and Electrical Properties of Graphene Oxide (GO) and Reduced Graphene Oxide (rGO)*. 2018.

[51] A. Teklu, C. Barry, M. Palumbo, C. Weiwadel, N. Kuthirummal, J. Flagg, Mechanical characterization of reduced graphene oxide using AFM, Adv. Condensed Matter Phys. 2019 (2019) 8713965, https://doi.org/10.1155/2019/8713965.

[52] K. Bilisik, M. Akter, Graphene nanocomposites: a review on processes, properties, and applications, J. Ind. Text. 51 (3_suppl) (2022) 3718S–3766S, https://doi.org/10.1177/15280837211024252.

[53] T. Hassenkam, L. Skovbjerg, S. Stipp, Probing the intrinsically oil-wet surfaces of pores in North Sea chalk at subpore resolution, Proc. Natl. Acad. Sci. U.S.A. 106 (2009) 6071–6076, https://doi.org/10.1073/pnas.0901051106.

[54] E.I. Rivin, E.I. Rivin, Introduction and Definitions. Handbook On Stiffness & Damping in Mechanical Design, ASME Press, 2010, p. 0.

[55] G. Thomas, N.A. Burnham, T.A. Camesano, Q. Wen, Measuring the mechanical properties of living cells using atomic force microscopy, J. Vis. Exp. (76) (2013), https://doi.org/10.3791/50497.

[56] G. Jayatilaka, W. Ntsoane, M. Mohammadi, M. Tehrani, Correlating Structure to Damping and Stiffness in Graphene Oxide Films, in: O. Zhupanska, E. Madenci (Eds.), American Society for Composites-Thirty-Seventh Technical Conference, DEStech Publications, Inc, Arizona, USA, 2022 [Online]. Available, https://par.nsf.gov/biblio/10416976.

[57] S. Iswar, et al., Dense and strong, but superinsulating silica aerogel, Acta Mater. 213 (2021) 116959, https://doi.org/10.1016/j.actamat.2021.116959.
[58] D.G. Papageorgiou, I.A. Kinloch, R.J. Young, Mechanical properties of graphene and graphene-based nanocomposites, Prog. Mater. Sci. 90 (2017) 75–127, https://doi.org/10.1016/j.pmatsci.2017.07.004.
[59] H.-J. Butt, B. Cappella, M. Kappl, Force measurements with the atomic force microscope: technique, interpretation and applications, Surf. Sci. Rep. 59 (1) (2005) 1–152, https://doi.org/10.1016/j.surfrep.2005.08.003.
[60] B. Cappella, Physical principles of force–distance curves by atomic force microscopy. Mechanical Properties of Polymers Measured Through AFM Force-Distance Curves, Springer International Publishing, Cham, 2016, pp. 3–66.
[61] D.L. Sedin, K.L. Rowlen, Adhesion forces measured by atomic force microscopy in humid air, Anal. Chem. 72 (10) (2000) 2183–2189, https://doi.org/10.1021/ac991198c.
[62] X. Zeng, Y. Peng, M. Yu, H. Lang, X.A. Cao, K. Zou, Dynamic sliding enhancement on the friction and adhesion of graphene, graphene oxide, and fluorinated graphene, ACS Appl. Mater. Interfaces 10 (9) (2018) 8214–8224, https://doi.org/10.1021/acsami.7b19518.
[63] R. Muzyka, S. Drewniak, T. Pustelny, M. Sajdak, Ł. Drewniak, Characterization of Graphite Oxide and Reduced Graphene Oxide Obtained from Different Graphite Precursors and Oxidized by Different Methods Using Raman Spectroscopy Statistical Analysis, Materials. (Basel) 14 (4) (2021), https://doi.org/10.3390/ma14040769.
[64] R. Zulkharnay, O. Ualibek, O. Toktarbaiuly, P.W. May, Hydrophobic behaviour of reduced graphene oxide thin film fabricated via electrostatic spray deposition, Bull. Mater. Sci. 44 (2) (2021) 112, https://doi.org/10.1007/s12034-021-02381-x.
[65] T. He, et al., Nanowrinkled Carbon Aerogels Embedded with FeNx Sites as Effective Oxygen Electrodes for Rechargeable Zinc-Air Battery, Research. 2019 (2019), https://doi.org/10.34133/2019/6813585.
[66] J.V. Escobar, C. Garza, R. Castillo, Measuring adhesion on rough surfaces using atomic force microscopy with a liquid probe, Beilstein J. Nanotechnol. 8 (2017) 813–825, https://doi.org/10.3762/bjnano.8.84.
[67] J. Dawson, et al., Dynamics of droplets impacting on aerogel, liquid infused, and liquid-like solid surfaces, ACS Appl. Mater. Interfaces 15 (1) (2023) 2301–2312, https://doi.org/10.1021/acsami.2c14483.
[68] H. Kang, et al., Studying the adhesion force and glass transition of thin polystyrene films by atomic force microscopy, Nanoscale Res. Lett. 13 (1) (2018) 5, https://doi.org/10.1186/s11671-017-2426-9.
[69] S.-C. Her, C.-Y. Huang, The effects of adhesive and bonding length on the strain transfer of optical fiber sensors, Appl. Sci. 6 (1) (2016) 13, https://doi.org/10.3390/app6010013.
[70] K.-K. Hung, I. Chasiotis, Control of substrate strain transfer to thin film photovoltaics via interface design, Solar Energy 225 (2021) 643–655, https://doi.org/10.1016/j.solener.2021.07.016.
[71] A.A. Osipov, High-temperature Raman spectroscopy, Pure Appl. Chem. 91 (11) (2019) 1749–1756, https://doi.org/10.1515/pac-2019-0115.
[72] Z.E. Brubaker, J.J. Langford, R.J. Kapsimalis, J.L. Niedziela, Quantitative analysis of Raman spectral parameters for carbon fibers: practical considerations and connection to mechanical properties, J. Mater. Sci. 56 (27) (2021) 15087–15121, https://doi.org/10.1007/s10853-021-06225-1.
[73] A.C. Ferrari, J. Robertson, Interpretation of Raman spectra of disordered and amorphous carbon, Phys. Rev. B 61 (20) (2000) 14095–14107, https://doi.org/10.1103/PhysRevB.61.14095.
[74] S. Claramunt, A. Varea, D. López-Díaz, M.M. Velázquez, A. Cornet, A. Cirera, The Importance of Interbands on the Interpretation of the Raman Spectrum of Graphene Oxide, J. Phys. Chem. C 119 (18) (2015) 10123–10129, https://doi.org/10.1021/acs.jpcc.5b01590.
[75] V. Georgakilas, et al., Functionalization of Graphene: covalent and Non-Covalent Approaches, Derivatives and Applications, Chem. Rev. 112 (11) (2012) 6156–6214, https://doi.org/10.1021/cr3000412.
[76] A. Eckmann, et al., Probing the Nature of Defects in Graphene by Raman Spectroscopy, Nano Lett. 12 (8) (2012) 3925–3930, https://doi.org/10.1021/nl300901a.
[77] T.M.G. Mohiuddin, et al., Uniaxial strain in graphene by Raman spectroscopy: g peak splitting, Gruneisen parameters, and sample orientation, Phys. Rev. B 79 (20) (2009) 205433, https://doi.org/10.1103/PhysRevB.79.205433.
[78] A.E. Mag-isa, J.-H. Kim, C.-S. Oh, Measurements of the in-plane coefficient of thermal expansion of freestanding single-crystal natural graphite, Mater. Lett. 171 (2016) 312–314, https://doi.org/10.1016/j.matlet.2016.02.110.
[79] Y. Su, et al., Exceptional negative thermal expansion and viscoelastic properties of graphene oxide paper, Carbon N Y 50 (8) (2012) 2804–2809, https://doi.org/10.1016/j.carbon.2012.02.045.
[80] A. Tardieu, F. Cansell, J.P. Petitet, Pressure and temperature dependence of the first-order Raman mode of diamond, J. Appl. Phys. 68 (7) (1990) 3243–3245, https://doi.org/10.1063/1.346375.
[81] H. Zhang, J. Horvat, Temperature dependence of Raman scattering spectroscopy in aerographite and single-walled carbon nanotube aerogel, Appl. Phys. A 127 (6) (2021) 434, https://doi.org/10.1007/s00339-021-04566-x.
[82] M.M. Shokrieh, S. Akbari, A. Daneshvar, Reduction of residual stresses in polymer composites using nano-additives, in: M.M. Shokrieh (Ed.), Residual Stresses in Composite Materials, Woodhead Publishing, 2014, pp. 350–373, ch. 13.
[83] D.G. Trikkaliotis, A.K. Christoforidis, A.C. Mitropoulos, G.Z. Kyzas, Graphene oxide synthesis, properties and characterization techniques: a comprehensive review, ChemEngineering 5 (3) (2021) 64, https://doi.org/10.3390/chemengineering5030064.
[84] V. Scardaci, G. Compagnini, Raman Spectroscopy Investigation of Graphene Oxide Reduction by Laser Scribing, C. (Basel) 7 (2) (2021) 48, https://doi.org/10.3390/c7020048.
[85] N.G. de Barros, et al., Graphene Oxide: a Comparison of Reduction Methods, C. (Basel) 9 (3) (2023) 73, https://doi.org/10.3390/c9030073.
[86] C. Neumann, et al., Raman spectroscopy as probe of nanometre-scale strain variations in graphene, Nat. Commun. 6 (1) (2015) 8429, https://doi.org/10.1038/ncomms9429.
[87] A.Y. Lee, et al., Raman study of D* band in graphene oxide and its correlation with reduction, Appl. Surf. Sci. 536 (2021) 147990, https://doi.org/10.1016/j.apsusc.2020.147990.
[88] D. López-Díaz, J.A. Delgado-Notario, V. Clericò, E. Diez, M.D. Merchán, M. M. Velázquez, Towards Understanding the Raman Spectrum of Graphene Oxide: the Effect of the Chemical Composition, Coatings 10 (6) (2020) 524, https://doi.org/10.3390/coatings10060524.
[89] J.A. Quezada Renteria, C. Ruiz-Garcia, T. Sauvage, L.F. Chazaro-Ruiz, J.R. Rangel-Mendez, C.O. Ania, Photochemical and electrochemical reduction of graphene oxide thin films: tuning the nature of surface defects, Phys. Chem. Chem. Phys. 22 (36) (2020) 20732–20743, https://doi.org/10.1039/D0CP02053B.
[90] H. Ramamoorthy, K. Buapan, T. Chiawchan, K. Thamkrongart, R. Somphonsane, Exploration of the temperature-dependent correlations present in the structural, morphological and electrical properties of thermally reduced free-standing graphene oxide papers, J. Mater. Sci. 56 (27) (2021) 15134–15150, https://doi.org/10.1007/s10853-021-06262-w.